C. R. Mecanique 346 (2018) 1018–1032

Contents lists available at ScienceDirect

Comptes Rendus Mecanique

www.sciencedirect.com

Computational methods in welding and additive manufacturing/Simulation numérique des procédés de soudage et de fabrication additive

Application of multi-phase viscoplastic material modelling to computational welding mechanics of grade-S960QL steel

Nicolas Häberle *, Andreas Pittner, Rainer Falkenberg, Ole Kahlcke, Michael Rethmeier

Bundesanstalt für Materialforschung und -prüfung (BAM), Unter den Eichen 87, 12205 Berlin, Germany

ARTICLE INFO

Article history:
Received 15 December 2017
Accepted 19 March 2018
Available online 23 August 2018

Keywords:
Computational welding mechanics
S960QL
Cyclic hardening
Viscoplasticity
Complex low-cycle fatigue test
Satoh test

ABSTRACT

The sound numerical prediction of welding-induced thermal stresses, residual stresses, and distortions strongly depends on the accurate description of a welded material's thermomechanical deformation behaviour. In this work, we provide experimental data on the viscoplastic deformation behaviour of a grade-S960QL steel up to a temperature of 1000 °C. In addition, a multi-phase viscoplastic material model is proposed, which accounts for the experimentally observed isothermal deformation behaviour of grade-S960QL steel base and austenitised material, as well as for athermal contributions that originate from solid-state phase transformations. The multi-phase viscoplastic and a classic rate-independent isotropic hardening material model were applied in the numerical simulations of both-ends-fixed bar Satoh tests and a single-pass gas metal arc weld. The influence of material modelling choices on the agreement between numerical simulation and experimental results is discussed, and recommendations for further work are given.

1. Introduction

The application of numerical methods to enhance the understanding and to facilitate the prediction of welding induced thermal stresses, residual stresses, and distortions is termed computational welding mechanics (CWM) [1]. One challenging aspect in CWM is the accurate description of the material thermomechanical deformation behaviour in the high-temperature region of the weld, where cyclic thermomechanical loading conditions do exist [2]. For high-strength low-alloy (HSLA) steels, such loading conditions result in a deformation behaviour with contributions by plastic strain hardening, viscoplasticity, and solid-state phase transformations [3]. The challenge to conduct in situ experimental measurements of thermal stresses and thermal strains in real welds led to the design of simplified experimental setups. A setup of particular interest for the validation of thermomechanical material modelling choices in CWM are both-ends-fixed bar Satoh [4] tests. Experimental Satoh tests and corresponding numerical simulations for low-alloy steels indicate that contributions of phase transformations by means of transformation-induced plasticity (TRIP) [5] must be accounted for, and recovery formulations of hardening state variables are recommended [6]. In addition, it was shown that taking into account viscoplastic effects [7], better suited plastic hardening formulations [6], and an improved description of phase transformation kinetics [8] favour the accurate numerical prediction of thermal stresses. Systematic investigations on material modelling choices in numerical simulations

* Corresponding author.
E-mail address: nicolas.haeberle@bam.de (N. Häberle).

https://doi.org/10.1016/j.crme.2018.08.001
1631-0721/

of real welds confirm the findings of the Satoh tests in terms of improved numerical predictions of residual stresses and distortions by considering viscoplastic effects [9,10], suitable plastic hardening formulations [11], and accurate modelling of solid-state phase transformations [8,12].

Grade-S960QL steel [13] exhibits a mixed isotropic softening/kinematic hardening deformation behaviour for cyclic plastic loading at ambient temperatures [8,14]. At elevated temperatures, low-alloy steels are known to harden kinematically with substantial contributions by viscoplastic effects. Contemporary hardening and viscoplastic formulations employed in CWM [3] offer a poor approximation to the deformation behaviour of grade-S960QL steel base and austenitised material. A more accurate description of the single-phase deformation behaviour of materials is accomplishable by the application of viscoplastic Chaboche [15] material models. Viscoplastic Chaboche models are not commonly employed in CWM, but are by now state of the art in numerical simulations of thermomechanically loaded structures such as extrusion toolings [16], internal combustion engine turbo chargers [17], or aero engines [18]. In regards to grade-S960QL steel, internal variables and corresponding evolution equations to describe nonlinear kinematic hardening [19] and strain-range memory effects [20,21] may be utilised to obtain a more accurate description of the material single-phase plastic strain hardening response. Short- and long-term contributions from viscoplastic effects are accessible by overstress and static recovery in hardening state variables [16,21]. To account for the contributions of solid-state phase transformations, Chaboche material models can be used in combination with the meso approach of Coret [22], which further incorporates the phenomenological Leblond phase kinetics model [23,24] and a rate-equation for TRIP strains [25,26]. Whereas the meso approach was not yet applied to CWM of an actual weld, promising results were obtained for the numerical simulation of a low-alloy steel during progressing solid-state phase transformations and the numerical rupture prediction of a nuclear pressure vessel subjected to accidental high-temperature loads [27]. The application of a Chaboche material model in combination with the meso approach, a Leblond phase kinetics model, and a TRIP rate equation in CWM demands a comprehensive set of experimental data in order to identify the models' parameters [28]. For grade-S960QL steel, experimental data sets available in the literature are limited to material strength in uni-axial cyclic loading at ambient temperatures [14], strength in uni-axial tension at elevated temperatures [29,30], the constant of TRIP strains for a fully martensitic transformation [31], some basic data on phase transformation kinetics [31,32], constants of elasticity and thermal material properties [30].

This work is a contribution to the experimental investigation and modelling of the grade-S960QL steel viscoplastic thermomechanical deformation behaviour with applications to CWM. Experimental data on the cyclic viscoplastic hardening response of the material as obtained in complex low-cycle fatigue (CLCF) tests [33] is provided up to a temperature of 1000 °C. We further provide experimental data on grade-S960QL steel thermal stresses and thermal strains in both-ends-fixed bar Satoh tests. A multi-phase viscoplastic material model which is based on the meso framework of Coret and the viscoplastic Chaboche material modelling approach is proposed and applied in the numerical simulations of the Satoh tests and a single-pass gas metal arc (GMA) weld. Alongside to the newly proposed model, a classic rate-independent isotropic hardening material model is applied in the numerical simulations. The consequences of material modelling choices on numerically predicted thermal stresses, thermal strains, and residual stresses are discussed by the comparison of the numerical simulation results and the experimental measurements. Suggestions for further work on material modelling of grade-S960QL steel in CWM are derived based on the reproducibility of experimental results in the corresponding numerical simulations.

2. Methodology – experimental investigations

2.1. Experimental complex low-cycle fatigue tests

The uniaxial viscoplastic cyclic hardening behaviour of grade-S960QL steel was experimentally investigated at isothermal conditions by CLCF tests [33]. The experimental setup and a schematic strain vs. time series of the strain-controlled CLCF tests is shown in Fig. 1(a) and (b). Each CLCF test did comprise three stages of strain amplitudes ε_1, ε_2, and ε_3, respectively. Each stage did consist of three cycles of tension/compression at strain rates $\dot{\varepsilon}_1 = 0.001\%/\mathrm{s}$ and $\dot{\varepsilon}_2 = 0.1\%/\mathrm{s}$, and one cycle at constant strain of dwell time t_h (stress relaxation cycle). The strain rates were identical for all temperatures of testing, with $\dot{\varepsilon}_1$ chosen slow enough to allow long-term static recovery to take place, and $\dot{\varepsilon}_2$ of a magnitude similar to the expected strain rates in the heat-affected zone (HAZ) and fusion zone (FZ) for a typical GMA weld. The remaining parameters of the CLCF tests (ε_1, ε_2, ε_3, t_h) were prescribed in dependence of the temperature of testing and are reproduced in Table 1. The strain amplitudes and dwell time were prescribed to aid parameter identification of the viscoplastic Chaboche model and to be representative for GMA welding. Temperatures of testing did span the range from 20 °C up to 1000 °C. In each CLCF test, the specimen was pre-heated at the temperature of testing for 30 min. Each test was repeated twice to confirm the reproducibility of the experimental results.

The geometry of the CLCF test specimens is shown in Fig. 2. All specimens were extracted from a 20-mm-thick WELDOX960E grade-S960QL steel plate in the direction of rolling. The chemical composition of the material is shown in Table 2. The surface finish of the specimens did correspond to smooth grinding. Two tensile testing machines were used in the CLCF campaign. CLCF tests up to and including 600 °C were conducted with an Instron 8561 servoelectrical computerised universal tensile testing machine where specimens were exposed to the atmosphere during testing. Testing at temperatures of 800 °C, 900 °C, and 1000 °C was realised with a MTS 810 servo hydraulic computerised universal tensile testing machine that was fitted with a vacuum chamber to shield the specimen in an argon 5.0 environment at a maximum 5 ppm of residual oxygen. The specimens were heated by electromagnetic induction in both setups. The temperature of the specimen

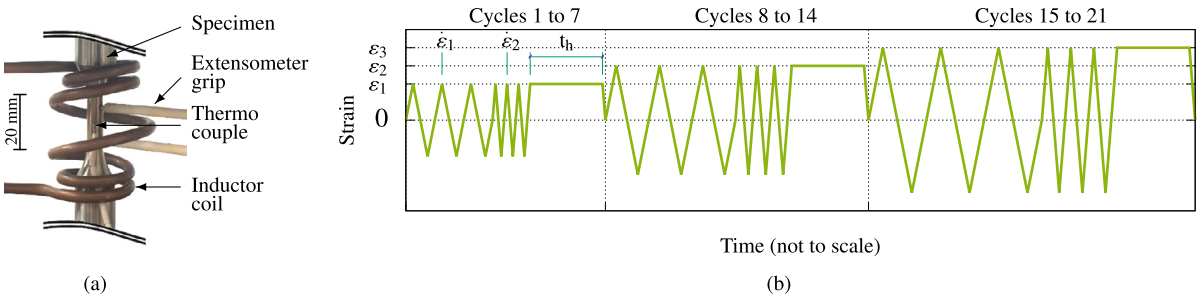

Fig. 1. Experimental setup of the CLCF tests (a), and schematic strain vs. time series (b).

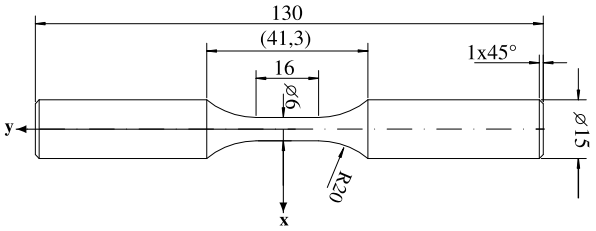

Fig. 2. CLCF specimen dimensions (in mm) and local coordinate system.

Table 1
Temperature dependent parameters of the CLCF test experiments.

T in °C	ε_1 in %	ε_2 in %	ε_3 in %	t_h in s
20.	0.51	0.85	1.2	3600.
200.	0.4	0.75	1.1	3600.
400.	0.33	0.665	1.	7200.
600.	0.14	0.47	0.8	7200.
800.	0.1	0.38	0.66	3600.
900.	0.08	0.33	0.58	3600.
1000.	0.06	0.28	0.5	3600.

Table 2
Maximum allowables (*) for grade-S960QL steel alloying elements in wt. % according to DIN EN 10025-6 [13] and SSAB test report data for CLCF test specimen material.

	C	Si	Mn	P	S	Cr	Ni	Mo	V	Ti	Cu	Al	Nb	B	N	Fe
DIN EN 10025-6*	.20	.80	1.70	.020	.010	1.5	2.0	.700	.120	.050	.50	> .015	.060	.005	.015	balance
SSAB test report	.16	.22	1.24	.010	.001	.20	.06	.603	.038	.003	.01	.055	.015	.001	.002	balance

was measured at $y = 0$ mm using a platinum/platinum–rhodium thermocouple of wire diameter 0.2 mm. Local straining of the specimen was measured by a MTS 632.51F-08-1147 extensometer calibrated to 5% elongation with extensometer rods applied at positions $y = -5$ mm and $y = +5$ mm.

2.2. Experimental Satoh tests

Satoh tests were conceived to investigate the evolution of thermal stresses in a material subjected to welding-like thermomechanical load histories by a both-ends-fixed bar analogy [4]. The specimens used in the experimental Satoh tests were identical to the CLCF test specimens and the experiments were conducted with the Instron 8561 tensile testing machine. Platinum/platinum–rhodium thermocouples were tack welded at $y = -10$ mm, $y = -5$ mm, $y = 0$ mm, $y = +5$ mm, $y = +10$ mm, $y = +15$ mm, and $y = +20$ mm to acquire temperature field data for the corresponding numerical simulation of the Satoh test. The extensometer setup was identical to the setup in the CLCF tests. The specimen was heated by electromagnetic induction with an inductor coil geometry for concentrated heat input. The temperature profile of the thermal cycles is (multi)linear in the heating stage, with peak temperatures of 706 °C and 908 °C. The peak temperatures correspond to material located in the non-austenitised and austenitised fine grain HAZ of a weld. The cooling part of the thermal cycles correspond to an experimental temperature measurement in the HAZ of a single-pass GMA weld without pre-heating. The applied heating rate is slow in comparison to a real GMA weld, but was necessary to avoid temperature oscillations related to the disposable heating control setup. Parts of the experimental setup and the prescribed thermal cycles are shown in

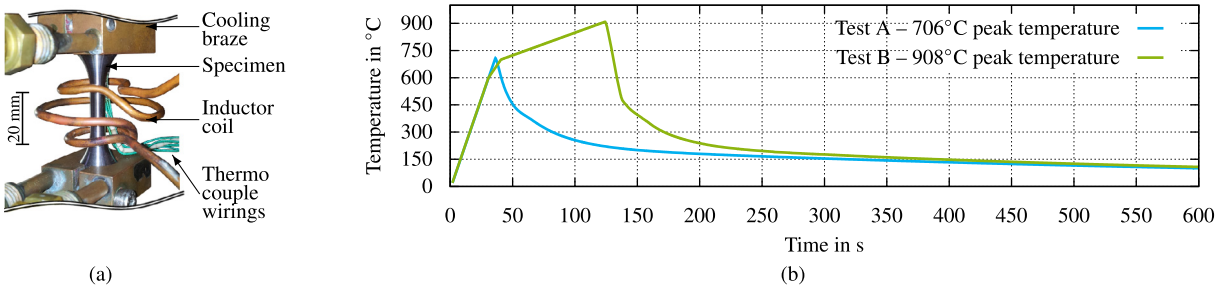

Fig. 3. Experimental setup of the SATOH tests – extensometer not shown (a). Prescribed temperature vs. time series (b).

Fig. 3(a) and (b). Water-cooled brass brazes as depicted in Fig. 3(a) were applied to the specimen to achieve sufficiently high cooling rates. The stroke of the tensile testing machine was kept constant during the Satoh tests according to the both-ends-fixed bar analogy.

3. Methodology – material modelling and numerical simulations

In this work, we follow the staggered approach where the thermometallurgical simulation is assumed not to be coupled with the thermomechanical simulation results. The thermometallurgical material model that describes the heat conduction properties and the phenomenological evolution of the metallurgical state in grade-S960QL steel is presented in section 3.1. The multi-phase viscoplastic and the classic rate-independent isotropic hardening material models that describe the material stress response for thermomechanical load paths that may involve solid-state phase transformations are presented in sections 3.2 and 3.3. The finite element models of the Satoh tests and the GMA weld are presented in section 3.4.

3.1. Thermometallurgical material model

The thermometallurgical material model specifies the effective specific heat capacity c, the effective heat conductivity λ, and the evolution of the metallurgical state $\mathbf{z}$ in a representative volume element (RVE) of material subjected to welding-like temperature histories. The metallurgical state $\mathbf{z}$ was introduced as a tuple of five scalars that denote the volume phase fractions of base material (z_1), martensite (z_2), bainite (z_3), ferrite (z_4), and austenite (z_5). The relationship $\sum_i z_i = 1$ holds. The effective specific heat capacity c and the effective heat conductivity λ for a mixture of metallurgical phases in a RVE of material was computed by the linear mixture rules

$$c(T) = \sum_i c_i(T)\, z_i \tag{1}$$

and

$$\lambda(T) = \sum_i \lambda_i(T)\, z_i \tag{2}$$

c_i and λ_i are the temperature-dependent specific heats and heat conductivities of the individual metallurgical phases. The effect of latent heat due to solidification, liquefaction, and solid-state phase transformations were neglected. In addition, dissipated heat caused by plastic deformations and the contributions from plastic deformations to a change of the metallurgical state were ignored. The evolution of the metallurgical state was described by the phenomenological Leblond phase kinetics model [23]. The influence of austenite grain conditioning on solid-state phase transformations was not modelled. Multi-linear parameterisations were employed to specify phase-transformation kinetics in the Leblond model, except for the austenite-to-martensite transformation, for which a modified version of the Koistinen–Marburger [8,24] relationship was used:

$$z_{\mathrm{eq}}(T) = 1 - \exp\left[-\beta \langle \mathrm{MS} - T \rangle^n\right] \tag{3}$$

In Eq. (3) T is the temperature in the RVE. MS, β, and n are material parameters that describe the martensite transformation characteristics. The Macaulay brackets for the scalar argument x are defined as $\langle x \rangle = (|x| + x)/2$. Eq. (3) results in the original Koistinen–Marburger relationship for $n = 1$.

The thermometallurgical material model was implemented in the ABAQUS6.12-3 FEM package using the UMATHT subroutine in order to solve for the temperature T and metallurgical state $\mathbf{z}$ in the numerical simulations of the Satoh tests and GMA weld.

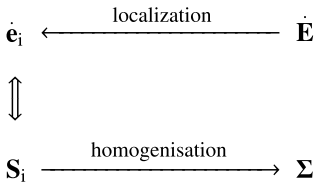

Fig. 4. Meso model localisation and homogenisation scheme. $\dot{\mathbf{E}}$ and $\boldsymbol{\Sigma}$ are the macroscopic strain rate and stress. $\dot{\mathbf{e}}_i$ and $\mathbf{S}_i$ are the phase specific (local) strain rates and stresses.

3.2. Multi-phase viscoplastic thermomechanical material model

The multi-phase viscoplastic deformation behaviour of grade-S960QL steel was described by the application of the meso model introduced by Coret [27] and a viscoplastic Chaboche [15] material modelling approach. In the meso approach, each RVE of material in a body is thought to consist of multiple metallurgical phases. The stress response in the i-th metallurgical phase is obtained by the application of a material model for a localised phase-specific strain rate $\dot{\mathbf{e}}_i$ and the macroscopic thermal loading condition of the RVE. The phase-specific localised strain rate is obtained by a localisation procedure from the macroscopic (total) strain rate $\dot{\mathbf{E}}$ in a RVE of material. The macroscopic state of stress $\boldsymbol{\Sigma}$ does result from the application of a homogenisation procedure in the stresses of the particular metallurgical phases $\mathbf{S}_i$. The localisation and homogenisation scheme is illustrated in Fig. 4.

In the multi-phase viscoplastic thermomechanical material model, we treat grade-S960QL steel as a two-phase material that consists of base material with volume phase fraction $1 - z_5$ and austenitised material with volume phase fraction z_5. The localisation procedure

$$\dot{\mathbf{e}}_i = \dot{\mathbf{E}} - \dot{\mathbf{E}}^{\mathbf{th}} - \dot{\mathbf{E}}^{\mathbf{tp}} \tag{4}$$

was used; it differs from the one proposed by Coret as the thermal strain rate of the RVE $\dot{\mathbf{E}}^{\mathbf{th}}$ is treated as macroscopic. $\dot{\mathbf{E}}^{\mathbf{tp}}$ is the rate of TRIP strains. The homogenisation procedure for the macroscopic state of stress $\boldsymbol{\Sigma}$ is a linear mixture rule in the stresses of the two metallurgical phases, and is identical to the formulation used by Coret,

$$\boldsymbol{\Sigma} = \sum z_i \mathbf{S}_i \tag{5}$$

The thermal strain rate in Eq. (4), $\dot{\mathbf{E}}^{\mathbf{th}}$, is the time derivative of

$$\mathbf{E}^{\mathbf{th}}(T) = \sum_i z_i \left[\alpha_i \left(T - T_{\mathrm{ref}}\right) + E^{\mathrm{th}}_{\mathrm{ref},i}\right] \mathbf{1} \tag{6}$$

Eq. (6) is a linear mixture rule for the RVE's macroscopic thermal strain in the thermal strains of the two metallurgical phases. The α_i are the coefficients of thermal expansion of the two metallurgical phases and T_{ref} is the reference temperature for thermal expansions of magnitude $E^{\mathrm{th}}_{\mathrm{ref},i}$. $\mathbf{1}$ is the unit tensor of rank 2. The rate of transformation-induced plastic strains $\dot{\mathbf{E}}^{\mathbf{tp}}$ in the localisation procedure, Eq. (4), was introduced as

$$\dot{\mathbf{E}}^{\mathbf{tp}} = 3\, K_{\mathrm{f}}\, \boldsymbol{\Sigma}' \left[z_5 \langle -\dot{z}_5 \rangle + (1 - z_5) \langle \dot{z}_5 \rangle\right] \tag{7}$$

In Eq. (7), K_{f} is the constant of transformation-induced plastic strains, which is a material parameter [31] and $\boldsymbol{\Sigma}'$ is the deviatoric part of the macroscopic state of stress in the RVE of the material. Eq. (7) is based on the common [5] parameterisation of TRIP strains in the segregating austenitic phase $\mathbf{E}^{\mathbf{tp}} = \frac{3}{2} K_f \Phi(z_5) \boldsymbol{\Sigma}'$ and the particular choice of the polynomial expression $\Phi = (1 - z_5)\left[2 - (1 - z_5)\right)]$. In this work, an identical TRIP characteristic was assumed for the formation and segregation of austenite. Eq. (7) then follows by taking the time derivative of $\mathbf{E}^{\mathbf{tp}}$ for the formation and segregation of austenite and for the assumption of a constant state of stress $\boldsymbol{\Sigma}'$ [5].

Eqs. (4) to (7) define the macroscopic multi-phase deformation behaviour for a RVE of material. The phase-specific thermomechanical deformation behaviour of grade-S960QL base and austenitised material was described by a viscoplastic Chaboche material model that was applied for each of the two metallurgical phases. Small deformations were assumed, and the stress in the i-th metallurgical phase $\mathbf{S}_i$ was assumed to be related to the elastic strain $\mathbf{e}^{\mathbf{e}}_i$ of the phase by Hooke's law. The strain rate in the i-th metallurgical phase $\dot{\mathbf{e}}_i$ was additively decomposed in an elastic $\dot{\mathbf{e}}^{\mathbf{e}}_i$ and plastic strain $\dot{\mathbf{e}}^{\mathbf{p}}_i$ component

$$\dot{\mathbf{e}}_i = \dot{\mathbf{e}}^{\mathbf{e}}_i + \dot{\mathbf{e}}^{\mathbf{p}}_i \tag{8}$$

A Norton-type overstress model as motivated in [15] was used to relate the plastic strain rate of the i-th phase, $\dot{\mathbf{e}}^{\mathbf{p}}_i$, to the phase specific state of stress $\mathbf{S}_i$ and phase specific state of kinematic $\mathbf{X}_i$ and isotropic hardening R_i,

$$\dot{\mathbf{e}}_i^{\mathbf{p}} = \frac{3}{2} \underbrace{\left\langle \frac{J_2\left(\mathbf{S}_i - \mathbf{X}_i\right) - \left(k_i + R_i\right)}{K_i} \right\rangle^{n_i}}_{\dot{\mathrm{p}}_\mathrm{i}} \frac{\mathbf{S'}_i - \mathbf{X}_i}{J_2\left(\mathbf{S}_i - \mathbf{X}_i\right)} \tag{9}$$

In Eq. (9), J_2 is the invariant $J_2(\mathbf{S}_i) = \sqrt{\frac{3}{2}\left(\mathbf{S}_i - \frac{1}{3}\mathrm{tr}\left(\mathbf{S}_i\right)\mathbf{1}\right) : \left(\mathbf{S}_i - \frac{1}{3}\mathrm{tr}\left(\mathbf{S}_i\right)\mathbf{1}\right)}$, where the scalar contraction of rank-two tensors is denoted by : and tr() is the trace operator. $\dot{\mathrm{p}}_\mathrm{i}$ is the equivalent plastic strain rate in the i-th phase. k_i, n_i and K_i are temperature dependent material parameters. $\mathbf{S'}_i$ is the deviatoric state of stress in the i-th metallurgical phase. The state of kinematic hardening in phase i, $\mathbf{X}_i$, was introduced as the sum of two back stress tensors

$$\mathbf{X}_i = \mathbf{X}_{i1} + \mathbf{X}_{i2} = \sum_{j=1}^{2} \mathbf{X}_{ij} \tag{10}$$

The relation of the back stress tensors $\mathbf{X}_{ij}$ to the back strain tensors $\mathbf{A}_{ij}$ and the corresponding evolution equations were adopted from [16] as

$$\mathbf{X}_{ij} = a_{ij}\,\mathbf{A}_{ij} \tag{11}$$

and

$$\dot{\mathbf{A}}_{ij} = c_{ij}\,\dot{\mathbf{e}}_i^{\mathbf{p}} - \frac{3}{2}\frac{c_{ij}}{a_{ij}}\mathbf{X}_{ij}\,\dot{p}_i - \frac{3}{2}d_{ij}\left(\frac{J_2\left(\mathbf{X}_{ij}\right)}{a_{ij}}\right)^{m_{ij}} \frac{\mathbf{X}_{ij}}{J_2\left(\mathbf{X}_{ij}\right)} - g(z_i, \dot{z}_i)\,\mathbf{A}_{ij} \tag{12}$$

with

$$g(z_i, \dot{z}_i) = \begin{cases} \frac{\langle \dot{z}_i \rangle}{z_i} & \text{if } z_i > 0 \\ 0 & \text{if } z_i = 0 \end{cases} \tag{13}$$

In Eqs. (11) and (12), a_{ij}, c_{ij}, d_{ij}, and m_{ij} are temperature-dependent material parameters of the i-th metallurgical phase and j-th kinematic hardening variable. The employed evolution equation for nonlinear kinematic hardening does comprise terms of linear kinematic hardening, dynamic recovery, static recovery, and annealing. The annealing formulation, Eq. (13), was introduced [6] to describe the effective state of hardening during an increase of the i-th metallurgical phase fraction. The formulation was derived in analogy with the effective austenite grain size formulation in the phase kinetics model of Leblond [23].

The phase-specific state of isotropic hardening R_i is also introduced based on the formulation of [16], with static recovery being neglected, but strain range memory effects and annealing due to phase transformations are accounted for:

$$R_i = Q_i\,r_i \tag{14}$$

$$\dot{r}_i = b_i\left(1 - r_i\right)\dot{p}_i - g(z_i, \dot{z}_i)\,r_i \tag{15}$$

In Eq. (15), Q_i and r_i are internal variables, b_i is a temperature-dependent material parameter. The internal variable Q_i describes the magnitude of isotropic softening/hardening in the presence of strain range memory effects [14,20,21]. Q_i was introduced as an extended version of the formalism presented in [21],

$$Q_i = Q_{0,i} + \left(Q_{m,i} - Q_{0,i}\right)\left[1 - \left[z_{i,1}\exp\left(-2\mu_{i,1}q_i\right) + z_{1,2}\exp\left(-2\mu_{i,2}q_i\right)\right]\frac{1}{z_{i,1} + z_{i,2}}\right] \tag{16}$$

$Q_{0,i}$, $Q_{m,i}$, $\mu_{i,1}$, $\mu_{i,2}$, $z_{i,1}$, $z_{i,2}$ are phase-specific temperature-dependent material parameters. q_i is a further phase-specific internal variable. The plastic strain memory surface,

$$F = \frac{2}{3}\,J_2\left(\mathbf{e}_i^{\mathbf{p}} - \boldsymbol{\xi}_i\right) - q_i \leq 0 \tag{17}$$

is used to describe strain range memory effects [21]. In Eq. (17), $\mathbf{e}_i^{\mathbf{p}}$ denotes the current plastic strain of the i-th phase and the internal variables $\boldsymbol{\xi}_i$ and q_i are state variables that describe a translation and expansion of the plastic-strain memory surface. The evolution equations of the internal variables $\boldsymbol{\xi}_i$ and q_i are

$$\dot{q}_i = \frac{2}{3}\,\eta_i\,H(F)\,\langle \mathbf{n}_i : \mathbf{n}_i^* \rangle\,\dot{p}_i - g(z_i, \dot{z}_i)\,q_i \tag{18}$$

$$\dot{\boldsymbol{\xi}}_i = \frac{2}{3}\left(1 - \eta_i\right)H(F)\,\langle \mathbf{n}_i : \mathbf{n}_i^* \rangle\,\dot{p}_i\,\mathbf{n}_i^* - g(z_i, \dot{z}_i)\,\boldsymbol{\xi}_i \tag{19}$$

In Eq. (18), $H(F)$ is the Heaviside step function, η_i is a temperature-dependent and phase-specific material parameter, and $\mathbf{n}_i$ is the phase-specific direction of the plastic flow, which follows from Eq. (9) as

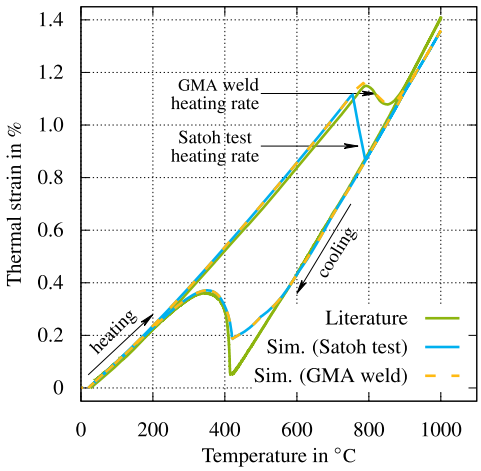

Fig. 5. Thermal strains in numerically simulated and experimental [31] grade-S960QL steel dilatometer tests. Austenitisation in the numerical model was assumed to depend on the heating rate. A bainitic/martensitic segregation of austenite was assumed on cooling.

$$\mathbf{n}_i = \frac{3}{2}\,\frac{\mathbf{S'}_i - \mathbf{X}_i}{J_2\left(\mathbf{S'}_i - \mathbf{X}_i\right)} \tag{20}$$

Furthermore, in Eq. (19), $\mathbf{n}_i^*$ is the normal to the plastic strain memory surface

$$\mathbf{n}_i^* = \frac{3}{2}\,\frac{\mathbf{e}_i^{\mathbf{p}} - \boldsymbol{\xi}_i}{J_2\left(\mathbf{e}_i^{\mathbf{p}} - \boldsymbol{\xi}_i\right)} \tag{21}$$

Eqs. (8) to (21) describe the thermomechanical deformation behaviour of the i-th phase; in combination with the meso model, Eqs. (4) to (7), they describe the multi-phase viscoplastic deformation behaviour of a RVE of material. The multi-phase viscoplastic material model was implemented in the ABAQUS6.12-3 FEM code using the UMAT subroutine for its application in the identification of material parameters [28] and in the numerical simulations of the Satoh tests and GMA weld.

3.3. Classic rate-independent isotropic hardening thermomechanical material model

The rate-independent isotropic hardening material model follows the classic approach in CWM. Hence, for small strains, the strain rate in a RVE of material is additively decomposed as the sum of an elastic, thermal, TRIP, and plastic part,

$$\dot{\mathbf{E}} = \dot{\mathbf{E}}^{\mathbf{e}} + \dot{\mathbf{E}}^{\mathbf{th}} + \dot{\mathbf{E}}^{\mathbf{tp}} + \dot{\mathbf{E}}^{\mathbf{p}} \tag{22}$$

The state of stress $\mathbf{S}$ and the elastic strains $\mathbf{E}^{\mathbf{e}}$ in a RVE of material are related by Hooke's law. The thermal and TRIP strain rates follow from Eqs. (6) and (7). The plastic strain rate $\dot{\mathbf{E}}^{\mathbf{p}}$ results from the isotropic hardening yield criterion

$$\sqrt{\frac{3}{2}\left(\mathbf{S}_{\mathrm{i}} - \frac{1}{3}\mathrm{tr}\left(\mathbf{S}_{\mathrm{i}}\right)\mathbf{1}\right) : \left(\mathbf{S}_{\mathrm{i}} - \frac{1}{3}\mathrm{tr}\left(\mathbf{S}_{\mathrm{i}}\right)\mathbf{1}\right)} - \sum z_i\, R_{\mathrm{f},i}\left(p_i\right) \leq 0 \tag{23}$$

where $R_{\mathrm{f},i}$ is the yield stress for the effective accumulated plastic strain $p_i = \int \dot{p}_i(\tau)\,\mathrm{d}\tau$ of the i-th metallurgical phase. τ is a measure of time. p_i is an effective measure of accumulated plastic strain as annealing was applied during an increase of the i-th metallurgical phase fraction. The material model was implemented in the ABAQUS6.12-3 FEM code using the UHARD, UEXPAN, USDFLD user, and the GETVRM utility subroutine.

3.4. Numerical model of the Satoh test and single-pass GMA weld

The thermometallurgical simulations of the Satoh tests and GMA weld were carried out with the ABAQUS6.12-3 FEM package. Volumetric heating was applied by the UDFLUX subroutine. Thermal material properties were applied according to [30]. Thermal properties of ferrite, bainite, martensite and base material were assumed to be equal. A mixed bainitic/martensitic segregation of austenite as depicted in Fig. 5 was assumed. The results obtained in the thermometallurgical simulation were transferred to the thermomechanical simulation by mapping. The thermomechanical simulations of the numerical models were conducted in ABAQUS using the C3D20R 20 node reduced integration 3D brick element. Thermomechanical material properties for the multi-phase viscoplastic material model were identified based on the experimental CLCF test results with a methodology motivated in [28]. Linear interpolation between the next lower and next higher material parameter set was employed to obtain material parameters at a given temperature T. The material properties were extrapolated for base

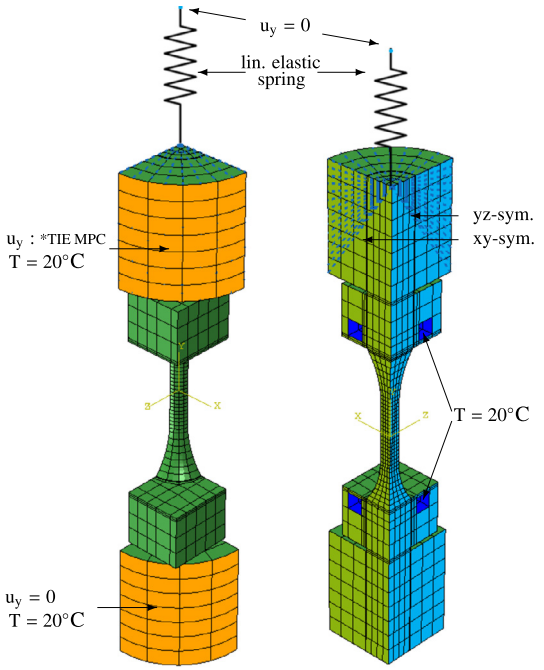

Fig. 6. Two views of the quarter model employed in the numerical simulation of the Satoh test. Regions of displacement **u** boundary conditions are coloured orange, light green, and light blue. Thermal boundary conditions on cooling channels are depicted dark blue. Multi point constraint couplings for nodes on the upper chuck chaw are shown as dashed lines.

material above 600 °C, and for austenitised material below 800 °C and above 1000 °C. Strength levels of hot tension test curves [30] were used as a guidance of material strength in the extrapolated temperature ranges. Material strength for the classic rate-independent isotropic hardening model was prescribed based on hot tension test curves of grade-S960QL steel [29,30]. The constant of transformation induced plastic strain for a pure martensitic transformation, $K_f = 6.9\ E^{-5}\,MPa^{-1}$, was used [31].

Fig. 6 shows the spatial discretisation and boundary conditions of the finite element Satoh test model. A quarter model with corresponding symmetry boundary conditions was employed. The specimen, cooling braces, and parts of the chuck chaws were incorporated in the spatial discretisation. Fixed displacement boundary conditions were applied for nodes on the outer surface of the lower chuck chaw. Nodes on the outer surface of the upper chuck chaw were tied to the lower end-point of a linear elastic spring. The spring was used to model the stiffness of the tensile testing machine and was prescribed as 56 GPa. The elastic stiffness of the cooling brazes was reduced according to the lose connection of the cooling brazes and the CLCF specimen in the experimental setup. The deformation behaviour of the chuck chaws was assumed to be linear elastic, with a stiffness of low alloy steel. Fixed temperature boundary conditions of 20 °C were applied on the outer surfaces of the chuck chaws and the cooling channel walls. Thermal boundary conditions of heat radiation and convective cooling were not applied. Heating of the specimen was modelled by a volumetric heat flux in material within $-25\ \text{mm} \leq y \leq +25\ \text{mm}$ of the specimen. The magnitude of heat input was computed based on the temperature difference between a target temperature and the temperature at the finite element integration points. The target temperature was a linear interpolation in the y-coordinate of the model with the experimental thermocouple measurements as sampling points. Only positive heat fluxes were allowed. Initial conditions were set to a temperature of 20 °C and a metallurgical state of pure base material.

The FEM model of the GMA weld is shown in Fig. 7. In the experimental weld, two grade-S960QL steel plates of 300 mm length, 60 mm width, and 6 mm thickness were joined in a single pass using a matching filler material. The joint plates were prepared with a V-groove. A half-model of the weld was used in the numerical simulation based on symmetry considerations. Multi point constraints were employed to constrain nodes in the regions of mesh refinements. The deposition of filler material during welding was modelled by the chewing gum method [1]. Chewing gum material properties were assigned to material in the V-groove, except for elements which were used to model the three tack welds. Chewing gum material properties were also applied for elements of deposited material on the weld root and weld toe. Heat input in the thermometallurgical simulation was modelled by a combination of ellipsoid heat sources [34]. The distribution and intensity of volumetric heat input was adjusted until the numerical simulation results did match experimental thermocouple measurements and the weld's FZ as obtained from macrographs. Convective and radiation cooling was applied to describe long-term cooling of the plate to ambient temperatures after welding. Initial conditions were set to 20 °C and pure base material in the welded plates. In the thermomechanical simulation, boundary conditions were applied to allow free shrinkage of the plate, see Fig. 7.

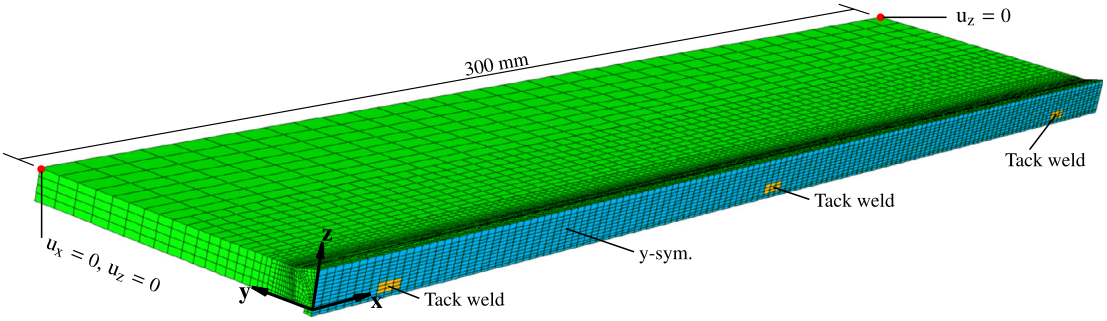

Fig. 7. Coordinate system, mesh, and mechanical displacement **u** boundary conditions for the numerical simulation of the single-pass weld. Symmetry displacement boundary conditions in regards to the *y*-plain were assumed for nodes on the blue (deposited filler material) and orange coloured (tack welds) element faces. The rigid body motion of the model was constraint by displacement boundary conditions at nodes highlighted by red dots. 33460 elements were used for the spatial discretisation of the plate.

4. Results and discussion

4.1. Experimental low-cycle fatigue tests and parameter identification of the viscoplastic Chaboche material model

CLCF test results were highly reproducible except for testing at 600 °C where the specimen stress response was only reproducible up to cycle 14. Cycles of a non-reproducible stress response were not considered for the identification of the Chaboche material model parameters and are excluded from the following presentation and discussion.

The cyclic hardening response of grade-S960QL steel in CLCF tests at 20 °C was in close agreement to experimental data provided in [8] and [14]. At 20 °C, a reduction of the elastic range did occur on first tensile plastic loading in cycles 1, 8, and 15. A stationary cyclic hardening response was obtained for the following five tension/compression cycles in each stage. Fig. 8(a) shows the stationary cyclic hardening response of the steel in cycles 6, 13, and 20. Fig. 8 (b) and (c) shows the softening response of the material during the first plastic loading at strain amplitudes ε_2 and ε_3. Isotropic softening was most pronounced in cycle 8. The effect of isotropic softening during cycles 1, 8, and 15 of the CLCF tests did diminish with increasing temperatures at 200 °C and 400 °C, and no isotropic softening did occur for testing at 600 °C. The stationary cyclic hardening stress response for tests at 200 °C and 400 °C is shown in Fig. 8(d) and (e). The cyclic hardening stress response did not depend on the strain rate at 200 °C. A pronounced contribution of viscoplastic effects on cyclic hardening was first observed in CLCF tests at 600 °C – see Fig. 8(f). Viscoplastic contributions by means of stress relaxation in grade-S960QL steel base material are shown in Fig. 9(a). A short-term stress relaxation did result in tests at 20 °C. For an increase in the temperature of testing, long-term viscoplastic effects did result, with a steady decrease of stress during the complete duration of the stress relaxation cycle.

The parameter identification of the Chaboche material model did result in a close description of the stationary cyclic hardening response of grade-S960QL base material, see Fig. 8(a) and (d)–(f). A good qualitative description of the material response did also result for combined isotropic softening/kinematic hardening, see Fig. 8(b) and (c). The contributions of viscoplastic effects on the material deformation behaviour are also well reproduced in the numerical simulations of the CLCF tests, Figs. 8(f) and 9(a). For the parameter identification of the Chaboche model, short-term viscoplastic effects at 20 °C were described by overstress. The stress relaxation response at elevated temperatures was described by overstress and static recovery of kinematic hardening state variables.

The cyclic hardening and stress relaxation response of grade-S960QL steel in austenitised conditions is shown in Fig. 10(a)–(c) and in Fig. 9(b). A kinematic hardening stress response with no isotropic hardening contributions did result. Viscoplastic contributions in terms of a strain-rate-dependent stress response in cyclic hardening and stress relaxation were distinctive. The experimentally observed deformation behaviour was properly reproduced after parameter identification of the viscoplastic Chaboche material model. As for the case of grade-S960QL steel base material, viscoplastic contributions were modelled by overstress and static recovery of kinematic hardening state variables.

4.2. Experimental Satoh tests and corresponding numerical simulations

The experimental Satoh test and corresponding numerical simulation results are shown in Fig. 11. The temperature cycle of Satoh's test A, Fig. 11(a), did lead to elastic loading of the specimen until the yield stress of grade-S960QL steel base material was reached at ≈ 550 °C, Fig. 11(c) and (e). The following plastic compression of the specimen at increasing temperatures did result in tensile residual stresses after cooling. The temperature cycle of Satoh's test B, Fig. 11(b), leads to an initially elastic loading, followed by plastic compression due to a decrease of the material strength up to AC1, and further plastic compression during austenitisation up to a temperature of $\approx$AC3 – see Fig. 11(d) and (f). On cooling, tensile thermal stresses did initially develop until the onset of solid-state phase transformations that lead to a decrease of thermal stresses caused by local thermal expansions and TRIP strains, both originating from the segregation of the austenitic phase. Tensile residual stresses of a magnitude similar to Satoh's test A did result after cooling to ambient temperatures.

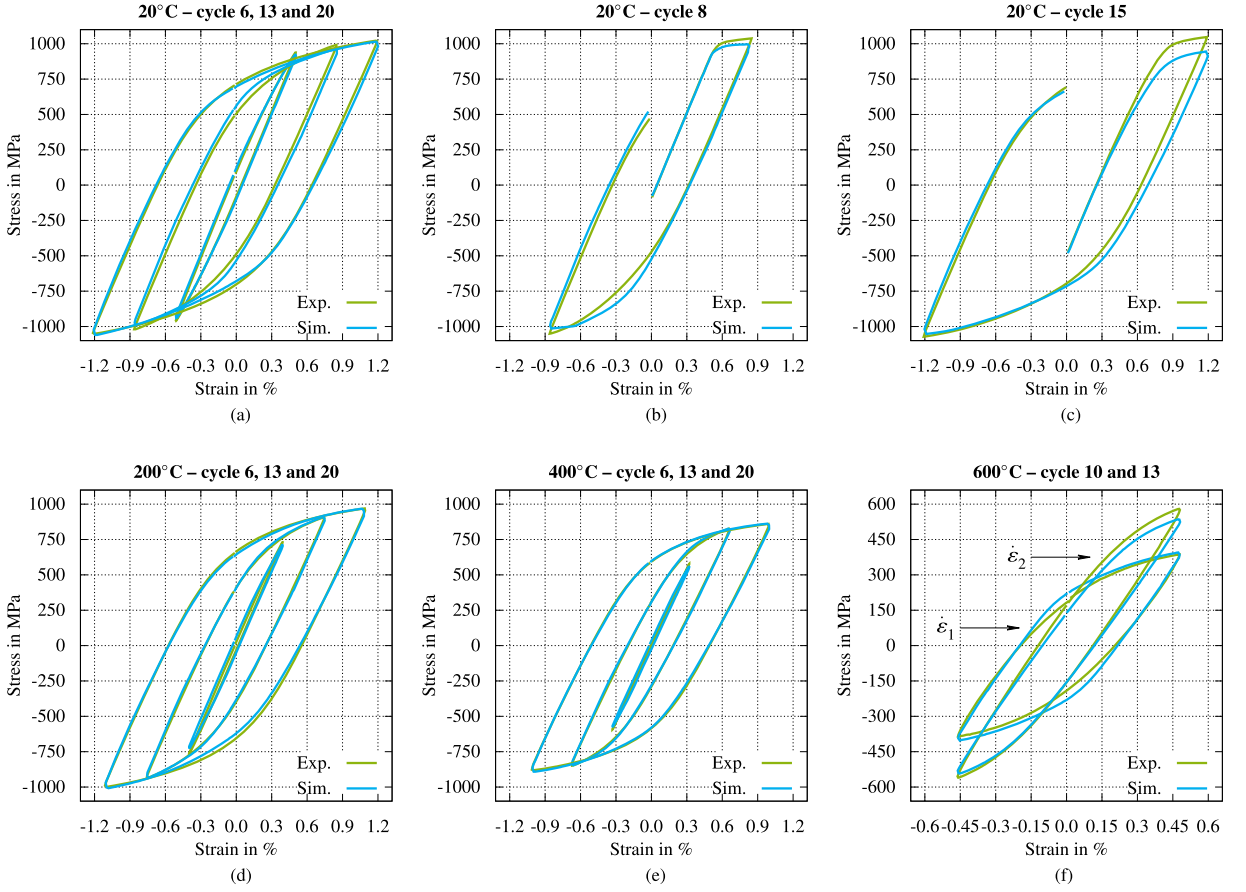

Fig. 8. Cyclic hardening stress response of grade-S960QL steel base material for temperatures of testing at 20 °C, 200 °C, 400 °C, and 600 °C. $\dot{\varepsilon}_1 = 0.001\%/s$, $\dot{\varepsilon}_2 = 0.1\%/s$.

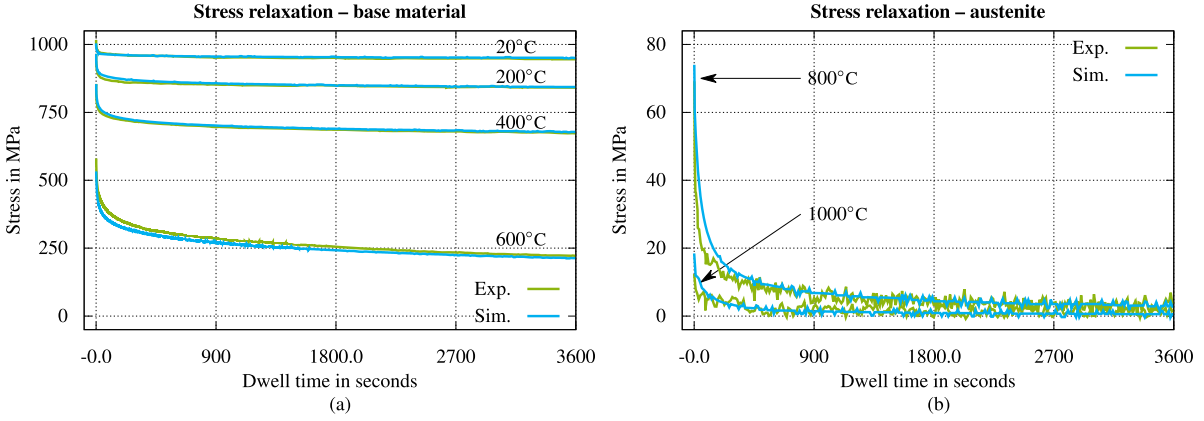

Fig. 9. Stress relaxation response of grade-S960QL steel base (a) and austenitised (b) material.

A good agreement of experimentally measured and numerically simulated temperature field data was obtained for both Satoh tests, Fig. 11(a) and (b). With regards to thermal stresses and strains, an equally good qualitative agreement did emerge for the application of both material models. However, a slightly better quantitative agreement of thermal stresses and strains was achieved by the application of the multi-phase viscoplastic material model.

The numerical simulation results of Satoh's test B indicate that both, classic and meso approach, offer an adequate representation of the multi-phase material deformation behaviour in CWM. The good agreement of thermal stresses and thermal strains for a progressive austenitisation of the specimen is favoured by accounting for TRIP strains during the formation as well as the segregation of the austenitic phase. The proper prediction of thermal stresses following partial

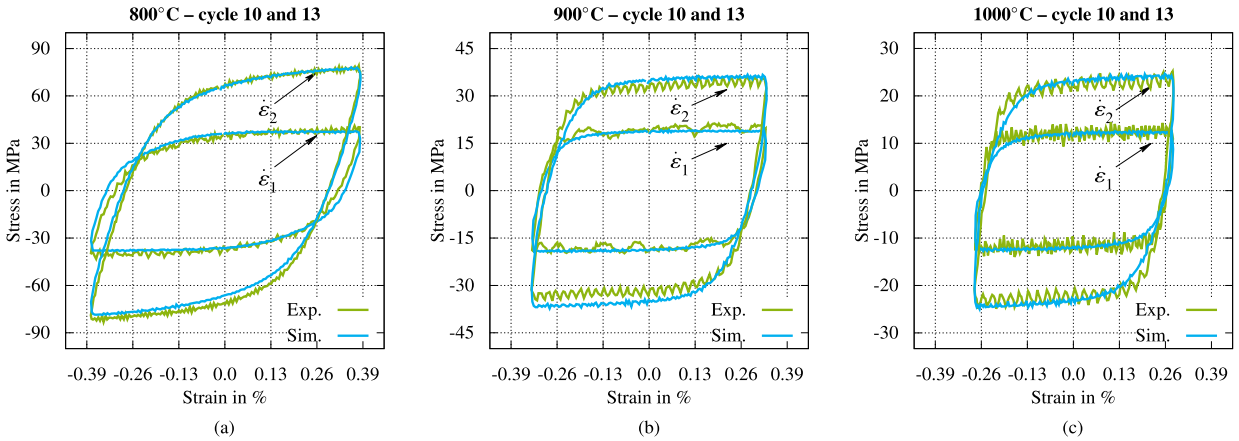

Fig. 10. Cyclic hardening stress response of grade-S960QL steel austenitised material for temperatures of testing at 800 °C, 900 °C, and 1000 °C. $\dot{\varepsilon}_1 = 0.001\%/s$, $\dot{\varepsilon}_2 = 0.1\%/s$.

austenitisation of the specimen further indicate that annealing formulations in hardening state variables during an increase in a metallurgical phase fraction do favour the accuracy of numerical simulation results, which is in agreement with findings in the literature [6].

It is worth noting that numerically simulated thermal stresses in both Satoh's tests are rarely affected by the employed viscoplastic and hardening formulation, which is in contrast to findings in the literature [6]. For Satoh's test A, this observation may be attributed to the high strength of grade-S960QL steel, which leads to elastic loading in tension after cooling from the peak temperature, so that no reverse plastic yielding does occur. In Satoh's test B, the thermal stress and thermal strain response is in large parts driven by the contributions from TRIP strains related to solid-state phase transformations. Hence, in both Satoh's tests, the plastic loading of base material is radial, a loading condition that is equally well described by the classic isotropic hardening and the Chaboche material modelling approach. Cyclic plastic loading is limited to the austenitised material in Satoh's test B – where the material response is indeed somewhat better predicted by the multi-phase viscoplastic modelling approach.

4.3. *Numerical simulation of the* GMA *weld*

Fig. 12 shows the Mises invariant and selected residual stress components in the GMA weld for a free body cut at half-length of the plate. Residual stresses of significant magnitude were confined to the HAZ of the weld. Longitudinal residual stresses of dominating intensity did evolve in non-austenitised base material spanning the complete thickness of the plate, Fig. 12(b). Transversal residual stresses of considerable magnitude did result in the transition region of non-austenitised and austenitised base material and are confined to the top and bottom surfaces of the plate, Fig. 12(c). Through thickness, residual stresses were limited to the transition region of non-austenitised and austenitised base material in the interior of the plate, Fig. 12(d).

The characteristic of the numerically predicted residual stress fields is very similar for the application of the classic and multi-phase viscoplastic material model. In particular, the distribution and magnitude of numerically predicted transverse and through-thickness residual stresses is virtually identical. However, longitudinal residual and Mises stresses of higher magnitude did result for the classic material modelling approach for non-austenitised base material in the HAZ of the weld. In this region of the weld, the non-austenitised base material is subjected to cyclic thermomechanical loading, which results in an isotropic softening/kinematic hardening deformation behaviour for the application of the multi-phase viscoplastic model. A more early plastic re-yielding in tension following a plastic compression results in the significantly lower magnitude of longitudinal residual stresses for the multi-phase viscoplastic model.

Fig. 13 shows a comparison of numerically predicted and experimentally measured residual stresses in the weld at $x = 150$ mm. In general, a good qualitative agreement was obtained for the application of both material models. Both modelling approaches reproduce the M-shape longitudinal residual stress profile that is typical for a single-pass HSLA steel weld. The application of the multi-phase viscoplastic material model did however result in a better prediction of longitudinal residual stress magnitudes. The level of longitudinal residual stresses was systematically overpredicted with the classic modelling approach in non-austenitised material close to the weld's austenitised zone. The overprediction of the longitudinal stress magnitude is related to the poor description of the grade-S960QL steel's cyclic hardening deformation behaviour by the isotropic hardening formulation. In terms of transversal residual stresses, a misprediction did result inside the austenitised zone (AZ) on the upper surface of the weld for both material modelling approaches. It is important to note that tensile residual stresses of high magnitudes in the austenitised zone of the weld necessarily need to develop after the segregation of the austenitic phase. High magnitudes of transversal thermal stresses in austenitised material would be offset by material expansion and TRIP strains during the austenite-to-bainite and martensite transformation – as it was the case for thermal

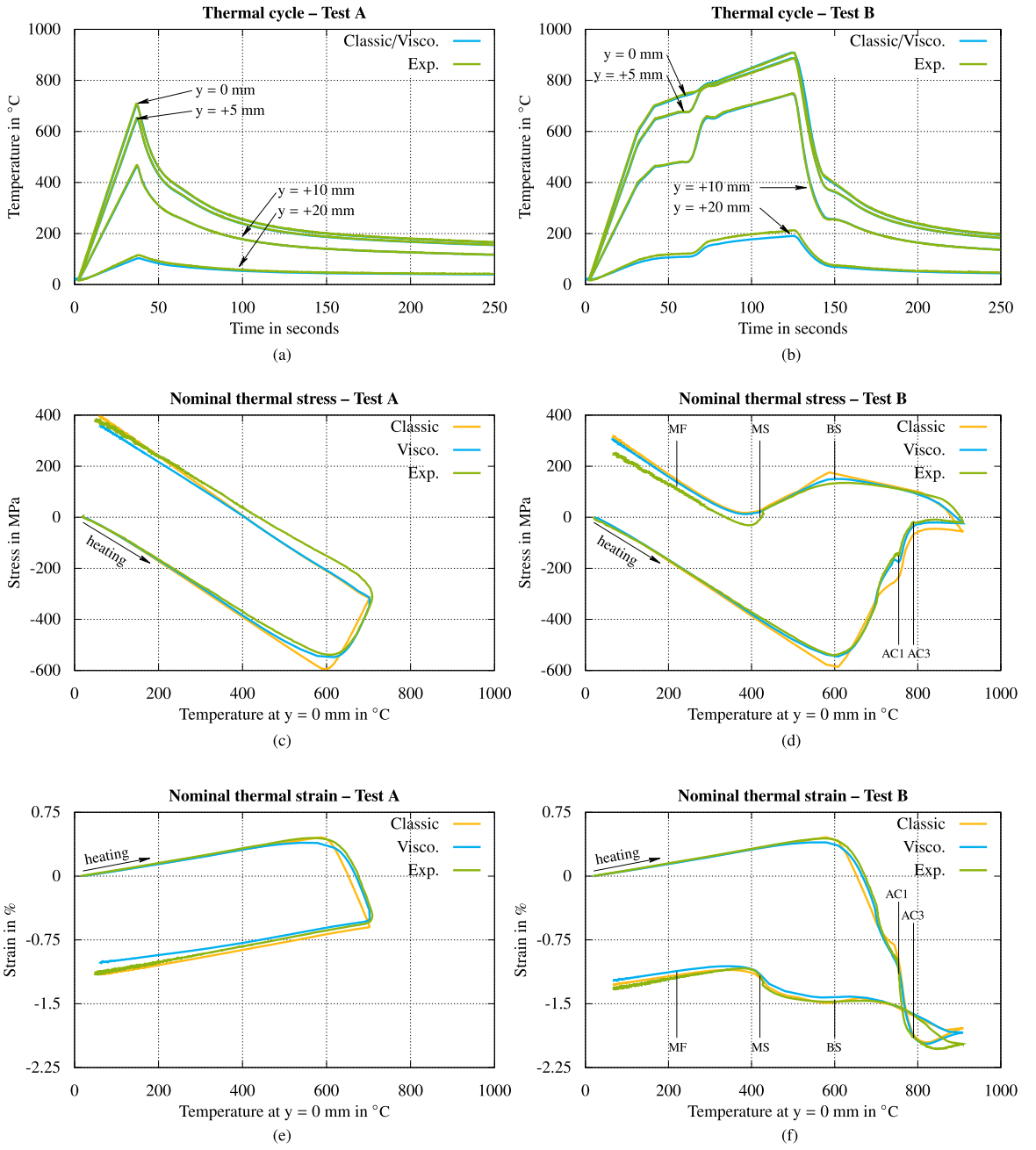

Fig. 11. Satoh test experimental and numerical results as obtained by the application of the rate independent isotropic hardening (Classic) and multi-phase viscoplastic (Visco.) material modelling approaches. AC1 and AC3 denote the austenite start and finish temperatures. BS and MS are the bainite and martensite start, MF is the martensite finish temperature.

stresses in Satoh's test B, Fig. 11(f). It is hence likely that a spatially varying onset of austenite segregation – possibly caused by austenite grain size effects – is a driving force for the experimentally measured tensile transversal residual stresses on the upper surface of the weld.

4.4. Recommendations for CWM *of grade-*S960QL *steel and suggestions for further work*

The numerical GMA weld results suggest that a proper description of the grade-S960QL steel's hardening response should be employed. The application of isotropic hardening or linear kinematic hardening formulations, which are commonly employed in CWM, are not suitable to describe the cyclic plastic hardening behaviour of the steel. Unfit hardening formulations result in mispredictions of residual stress magnitudes for material subjected to cyclic plastic loading in the HAZ of the

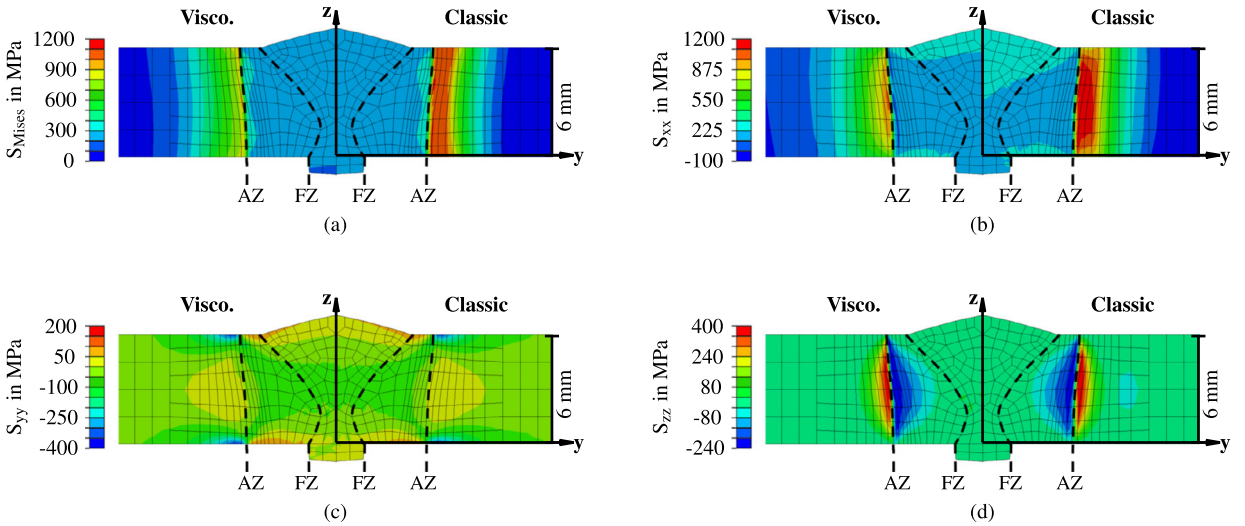

Fig. 12. Numerically predicted Mises (a), longitudinal (b), transversal (c), and through-thickness residual stresses (d) in the single-pass GMA weld at $x = 150$ mm. AZ and FZ mark the extent of the austenitised and fusion zones. Visco. denotes results obtained from the multi-phase viscoplastic simulation, Classic denotes results obtained with the rate-independent isotropic hardening model.

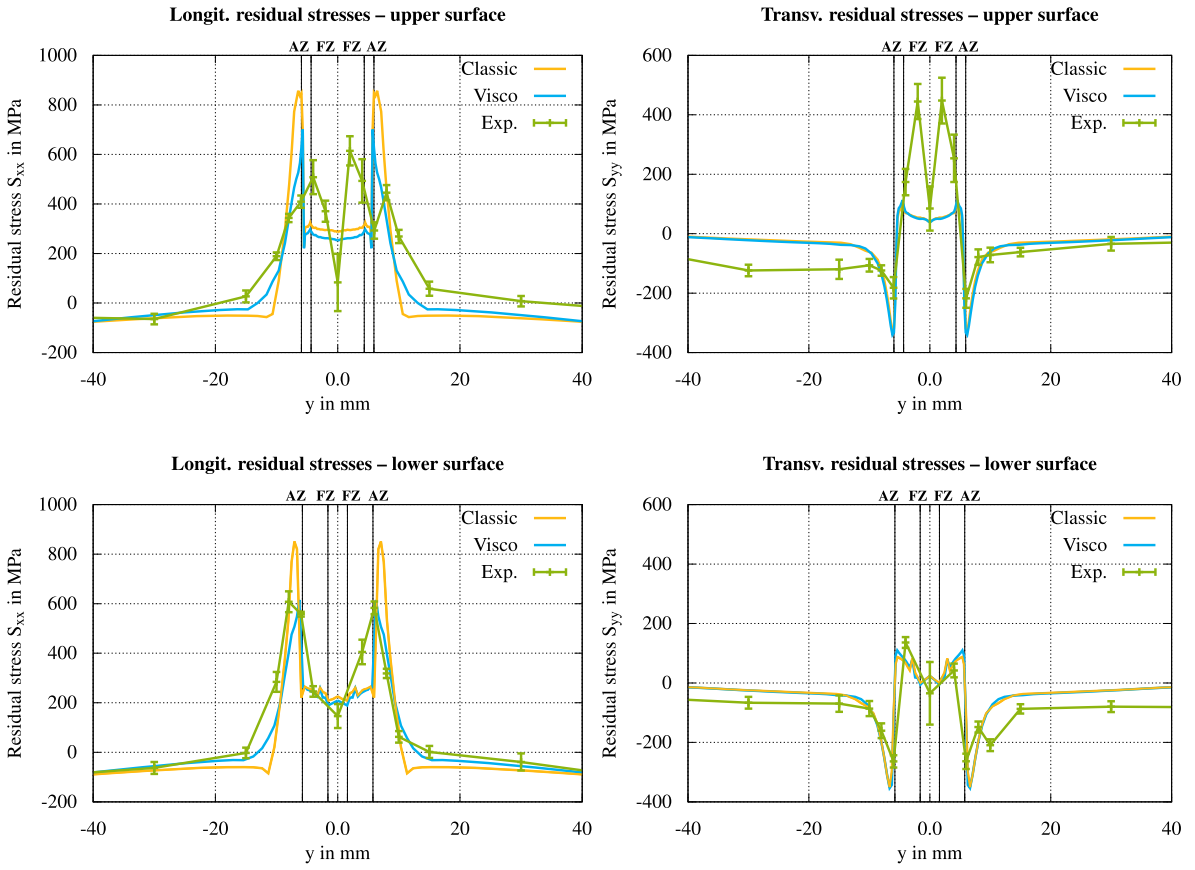

Fig. 13. Comparison of numerically predicted and experimentally measured (X-ray diffraction) longitudinal (S_{xx}) and transversal (S_{yy}) residual stresses on the upper and lower surfaces of the weld at $x = 150$ mm. AZ and FZ denote the extent of the austenitised and fusion zone of the weld.

weld. Whereas the region of the material subjected to cyclic thermomechanical loading conditions is confined in single-pass welds, a more severe misprediction of residual stresses is to be expected in numerical simulations of multi-pass welds that feature a larger HAZ and multiple thermomechanical load cycles in HAZ material.

Considering viscoplastic effects did not significantly improve the numerical predictions of thermal stresses and thermal strains in the Satoh tests or residual stresses in the single-pass GMA weld. However, taking into account viscoplastic effects via overstress and static recovery of hardening state variables might prove worthwhile in numerical simulations of multi-pass welding, post-weld heat treatments, or welded structures subjected to accidental high-temperature loads.

The contribution of solid-state phase transformations on the material thermomechanical deformation behaviour is significant, which is readily obvious in Satoh's test B – see Fig. 11(d). At the same time, no experimental data on grade-S960QL steel solid-state phase transformations for varying austenitisation conditions and cooling cycles are available. Further work in terms of experimental investigations and modelling of phenomenological solid-state phase transformation kinetics of grade-S960QL steel is expected to further improve numerically predicted thermal and residual stresses.

5. Summary and conclusions

The cyclic viscoplastic hardening behaviour of grade-S960QL steel was experimentally investigated. A multi-phase viscoplastic material model that describes the experimentally observed deformation behaviour of the steel in close approximation was proposed. The newly proposed model and a classic material model were applied in CWM of grade-S960QL steel. Both models were found suitable to reproduce the vast majority of experimental results with an improved numerical prognosis of thermal stresses, thermal strains, and residual stresses for the application of the multi-phase viscoplastic model. Based on the agreement and deviation of experimental and numerical results, we can draw the following conclusions.

- Viscoplastic Chaboche models are suitable to describe the uni-axial cyclic viscoplastic hardening deformation behaviour of grade-S960QL steel base and austenitised material with a good approximation.
- The meso approach of Coret allows for the application of viscoplastic Chaboche material models for materials subjected to solid-state phase transformations. The effect of solid-state phase transformations on the material deformation behaviour is equally well accounted for in the meso and classic material modelling approaches.
- A proper description of the grade-S960QL cyclic hardening behaviour favours the sound numerical prediction of residual stress levels in non-austenitised base material in the HAZ of a single-pass weld.
- The description of viscoplastic effects may increase the accuracy of numerically predicted thermal stresses and strains. However, the gain in accuracy by viscoplastic formulations for the application to a single-pass GMA weld was small compared to the gain in accuracy that did result from improved cyclic hardening formulations.
- Further work in CWM of grade-S960QL steel should focus on experimental investigations and modelling of the phenomenological nature of solid-state phase transformations. This should include effects of austenite grain size and cooling conditions.

References

[1] L.-E. Lindgren, Finite element modeling and simulation of welding, part 1: increased complexity, J. Therm. Stresses 24 (2) (2001) 141–192.
[2] D. Radaj, Heat Effects of Welding: Temperature Field, Residual Stress, Distortion, Springer-Verlag, 1992.
[3] L.-E. Lindgren, Finite element modeling and simulation of welding. Part 2: improved material modeling, J. Therm. Stresses 24 (3) (2001) 195–231.
[4] K. Satoh, Transient thermal stresses of weld heat-affected zone by both-ends-fixed bar analogy, Trans. Jpn. Weld. Soc. 3 (1) (1972) 125–134.
[5] F. Fischer, Q.-P. Sun, K. Tanaka, Transformation-induced plasticity (TRIP), Appl. Mech. Rev. 49 (6) (1996) 317–364.
[6] Y. Vincent, J.-F. Jullien, P. Gilles, Thermo-mechanical consequences of phase transformations in the heat-affected zone using a cyclic uniaxial test, Int. J. Solids Struct. 42 (14) (2005) 4077–4098.
[7] Y. Vincent, J.-M. Bergheau, J.-B. Leblond, Viscoplastic behaviour of steels during phase transformations, C. R. Mecanique 331 (9) (2003) 587–594.
[8] Y. Li, H. Lu, C. Yu, Y. Wu, Accurate prediction of welding stress evolution by considering improved phase transformation model, Mater. Trans. 56 (5) (2015) 715–719.
[9] J.-M. Bergheau, Y. Vincent, J.-B. Leblond, J.-F. Jullien, Viscoplastic behaviour of steels during welding, Sci. Technol. Weld. Join. 9 (4) (2004) 323–330.
[10] Z. Moumni, F. Roger, N.T. Trinh, Theoretical and numerical modeling of the thermomechanical and metallurgical behavior of steel, Int. J. Plast. 27 (3) (2011) 414–439.
[11] T. Schenk, I. Richardson, G. Eßer, M. Kraska, Influence of the Hardening Model on the Predicted Welding Distortion of DP600 Lap Joints, Materials Science Forum, vol. 638, Trans. Tech. Publ., 2010, pp. 3710–3715.
[12] A.S. Oddy, J.A. Goldak, J.M.J. McDill, Transformation effects in the 3D finite element analysis of welds, in: Proceedings of the Second International Conference on Trends in Welding Research, 1989, pp. 15–19.
[13] DIN EN 10025-6, Hot rolled products of structural steels – part 6: technical delivery conditions for flat products of high yield strength structural steels in the quenched and tempered conditions, DIN Deutsches Institut für Normung e. V., Berlin, Germany, 2013.
[14] L. Fu, C. Deng, H. Ren, Y. Zhong, H. Zhou, A Modified Yoshida–Uemori Constitutive Model and Its Application to Cold-Bending in Weldox960, Advanced Materials Research, vol. 834, Trans. Tech. Publications, Switzerland, 2014, pp. 407–415.
[15] J.-L. Chaboche, A review of some plasticity and viscoplasticity constitutive theories, Int. J. Plast. 24 (10) (2008) 1642–1693.
[16] C. Sommitsch, R. Sievert, T. Wlanis, B. Günther, V. Wieser, Modelling of creep-fatigue in containers during aluminium and copper extrusion, Comput. Mater. Sci. 39 (1) (2007) 55–64.
[17] J. Schicker, R. Sievert, B. Fedelich, H. Klingelhöffer, B. Skrotzki, Failure estimation of thermo-mechanically loaded hot parts in turbochargers, MTZ Worldw. 71 (6) (2010) 48–53.
[18] U. Müller, K. Höschler, M. Gerendas, H.-J. Bauer, U. Schoth, Mechanical analysis of an aero-engine combustor under operation conditions using a unified constitutive material model for deformation simulation, in: Proceedings of the International Conference on Temperature-Fatigue Interaction, Elsevier, 2001, pp. 351–360.

[19] P.J. Armstrong, C.O. Frederick, A Mathematical Representation of the Multiaxial Bauschinger Effect, Central Electricity Generating Board [and] Berkeley Nuclear Laboratories, Research & Development Department, Berkeley, CA, USA, 1966.
[20] J.-L. Chaboche, K. Van Dang, G. Cordier, Modelization of the strain memory effect on the cyclic hardening of 316 stainless steel, in: Structural Mechanics In Reactor Technology Transactions, 1979.
[21] J.-L. Chaboche, A. Gaubert, P. Kanouté, A. Longuet, F. Azzouz, M. Mazière, Viscoplastic constitutive equations of combustion chamber materials including cyclic hardening and dynamic strain aging, Int. J. Plast. 46 (2013) 1–22.
[22] M. Coret, A. Combescure, A mesomodel for the numerical simulation of the multiphasic behavior of materials under anisothermal loading (application to two low-carbon steels), Int. J. Mech. Sci. 44 (9) (2002) 1947–1963.
[23] J.-B. Leblond, J. Devaux, A new kinetic model for anisothermal metallurgical transformations in steels including effect of austenite grain size, Acta Metall. 32 (1) (1984) 137–146.
[24] D. Koistinen, R. Marburger, A general equation prescribing the extent of the austenite–martensite transformation in pure iron–carbon alloys and plain carbon steels, Acta Metall. 7 (1) (1959) 59–60.
[25] J.-B. Leblond, J. Devaux, J.-C. Devaux, Mathematical modelling of transformation plasticity in steels I: case of ideal-plastic phases, Int. J. Plast. 5 (6) (1989) 551–572.
[26] J.-B. Leblond, Mathematical modelling of transformation plasticity in steels II: coupling with strain hardening phenomena, Int. J. Plast. 5 (6) (1989) 573–591.
[27] M. Coret, Étude expérimentale et simulation de la plasticité de transformation et du comportement multiphase de l'acier de cuve 16MND5 sous chargement multiaxial anisotherme, Ph.D. thesis, École normale supérieure, Cachan, France, 2001.
[28] Z.-L. Zhan, J. Tong, A study of cyclic plasticity and viscoplasticity in a new nickel-based superalloy using unified constitutive equations. Part I: evaluation and determination of material parameters, Mech. Mater. 39 (1) (2007) 64–72.
[29] X. Qiang, X. Jiang, F.S.K. Bijlaard, H. Kolstein, Mechanical properties and design recommendations of very high strength steel S960 in fire, Eng. Struct. 112 (2016) 60–70.
[30] S. Neubert, A. Pittner, M. Rethmeier, Numerical sensitivity analysis of TRIP-parameter K on welding residual stresses for high-strength low-alloyed steels, J. Therm. Stresses 39 (2) (2016) 201–219.
[31] S. Neubert, A. Pittner, M. Rethmeier, Experimental determination of TRIP-parameter K for mild-and high-strength low-alloy steels and a super martensitic filler material, SpringerPlus 5 (1) (2016) 754.
[32] T. Slezak, J. Zmywaczyk, P. Koniorczyk, L. Sniezek, DSC investigations of the phase transition in the high strength steel S960QL, Adv. Mater. Res. 1126 (2015) 148–154.
[33] T. Seifert, Ein komplexes LCF-Versuchsprogramm zur schnellen und günstigen Werkstoffparameteridentifizierung, in: Proceedings of Werkstoffprüfung, 2006, pp. 409–414.
[34] J. Goldak, A. Chakravarti, M. Bibby, A new finite element model for welding heat sources, Metall. Trans. B 15 (2) (1984) 299–305.